The Astrophysical Journal, 752:64 (13pp), 2012 June 10 doi:10.1088/0004-637X/752/1/64

A *WISE* VIEW OF A NEARBY SUPERCLUSTER A2199

Ho Seong Hwang[1], Margaret J. Geller[1], Antonaldo Diaferio[2,3], and Kenneth J. Rines[4]
[1] Smithsonian Astrophysical Observatory, 60 Garden Street, Cambridge, MA 02138, USA; hhwang@cfa.harvard.edu, mgeller@cfa.harvard.edu
[2] Dipartimento di Fisica, Università degli Studi di Torino, V. Pietro Giuria 1, 10125 Torino, Italy; diaferio@ph.unito.it
[3] Istituto Nazionale di Fisica Nucleare (INFN), Sezione di Torino, V. Pietro Giuria 1, 10125 Torino, Italy
[4] Department of Physics and Astronomy, Western Washington University, Bellingham, WA 98225, USA; kenneth.rines@wwu.edu
Received 2012 February 15; accepted 2012 April 11; published 2012 May 25

ABSTRACT

We use *Wide-field Infrared Survey Explorer* (*WISE*) data covering the entire region ($\sim$130 deg^2) of the A2199 supercluster at $z = 0.03$ to study the mid-infrared (MIR) properties of supercluster galaxies. We identify an "MIR star-forming sequence" in the *WISE* [3.4]–[12] color–12 μm luminosity diagram, consisting of late-type, star-forming galaxies. At a fixed star formation rate, the MIR-detected galaxies at 22 μm or 12 μm tend to be more metal-rich and to have higher surface brightness than those without MIR detection. Using these MIR-detected galaxies, we construct the IR luminosity function (LF) and investigate its environmental dependence. Both total IR (TIR) and 12 μm LFs are dominated by late-type, star-forming galaxies. The contribution of active galactic nucleus host galaxies increases with both TIR and 12 μm luminosities. The contribution of early-type galaxies to the 12 μm LFs increases with decreasing luminosity. The faint-end slope of the TIR LFs does not change with environment, but the change of faint-end slope in the 12 μm LFs with the environment is significant: there is a steeper faint-end slope in the cluster core than in the cluster outskirts. This steepening results primarily from the increasing contribution of early-type galaxies toward the cluster. These galaxies are passively evolving, and contain old stellar populations with weak MIR emission from the circumstellar dust around asymptotic giant branch stars.

Key words: galaxies: clusters: individual (Abell 2199) – galaxies: evolution – galaxies: formation – galaxies: luminosity function, mass function – infrared: galaxies

Online-only material: color figures

1. INTRODUCTION

Galaxy properties including morphology, star formation rate (SFR), color, and activity in galactic nuclei are strongly affected by the environment (see Blanton & Moustakas 2009 for a review). The galaxy cluster environment is special because it contains the intracluster medium (ICM), galaxies, and dark matter that affect galaxy properties gravitationally and/or hydrodynamically over several billion years. For example, the typical morphology (also SFR, color, and activity in galactic nuclei) of galaxies changes with both local density and clustercentric radius (e.g., Oemler 1974; Davis & Geller 1976; Dressler 1980; Park & Hwang 2009; Hwang et al. 2012). This environmental dependence of galaxy properties in galaxy clusters may result from a host of physical mechanisms including ram pressure (Gunn & Gott 1972), cumulative galaxy–galaxy hydrodynamic/gravitational interactions (Park & Hwang 2009), strangulation (Larson et al. 1980), and galaxy harassment (Moore et al. 1996) (see Boselli & Gavazzi 2006; Park & Hwang 2009 for a review).

One of the fundamental tools for understanding the physics of morphological transformation and the quenching of star formation activity (SFA) is the galaxy luminosity function (LF; Blanton et al. 2001; Benson et al. 2003; Park et al. 2007; Rines & Geller 2008; Geller et al. 2012). LFs in infrared (IR) bands can provide an unbiased view of SFA in cluster galaxies because they are insensitive to dust extinction (e.g., Gallazzi et al. 2009; Haines et al. 2011).

Since the pioneering work on IR observations of cluster galaxies with *Infrared Astronomical Satellite* (*IRAS*) and *Infrared Space Observatory* (*ISO*; see Metcalfe et al. 2005 for a review), there have been several determinations of the IR LFs for cluster galaxies with recent IR satellites including the *Spitzer Space Telescope* (Werner et al. 2004), *AKARI* (Murakami et al. 2007), and the *Herschel Space Observatory* (Pilbratt et al. 2010). For example, Bai et al. (2006, 2009) use extensive *Spitzer* observations of local galaxy clusters including Coma and A3266 to conclude that IR LFs are well fitted with the Schechter (1976) function. They suggest that the bright end of IR LFs for local rich clusters has a universal form, similar to the LFs for nearby field galaxies. Tran et al. (2009) confirmed this universal form of IR LFs in Cl1358 at $z = 0.33$; other studies confirmed it in A2255 at $z = 0.08$ (Shim et al. 2011) and in the Shapley supercluster (Haines et al. 2011).

Studies of other clusters yield surprisingly different results: there is an excess of bright IR sources in the bullet cluster at $z = 0.3$ (Chung et al. 2010) and an excess of faint IR sources in the A1763 supercluster at $z = 0.23$ (Biviano et al. 2011).

The environmental dependence of IR LFs remains an open question. For example, Bai et al. (2009) suggest that the cluster and field IR LFs do not seem to differ significantly from one another (see also Finn et al. 2010; Haines et al. 2011). However, Bai et al. (2006) found a hint of a steeper faint-end slope toward the outer region of the Coma cluster. Tran et al. (2009) also found an excess of bright IR sources in their LF of the super group (SG1120) at $z = 0.37$ compared to that of field galaxies at similar redshift (see also Atlee & Martini 2012). Biviano et al. (2011) found that the slopes of IR LFs in three different regions in the A1763 supercluster (i.e., the cluster core, the large-scale filament, and the cluster outskirts) are similar, but the filament appears to have a flatter LF than both the outskirts and the core.

Here, we discuss the IR LFs for galaxies in the A2199 supercluster. This supercluster is one of the best targets for the study of IR LFs and their environmental dependence because the entire supercluster region ($R \lesssim 10\,h^{-1}$ Mpc) is uniformly covered by the *Wide-field Infrared Survey Explorer* (*WISE*; Wright et al. 2010) with excellent sensitivity at mid-IR (MIR) wavelengths.

This region is also fully covered by the Sloan Digital Sky Survey (SDSS; York et al. 2000) as well as by other large spectroscopic surveys. Thus, ambiguity in determining cluster membership is vastly reduced. To understand the behavior of the LFs in the supercluster, we also explore the MIR colors of galaxies focusing on the connection to IR luminosities and their environmental dependence.

A2199 is a regular, X-ray bright, rich galaxy cluster at $z \sim 0.03$, and forms a supercluster with several nearby groups in the infall region including A2197W and A2197E (Rines et al. 2001). The center of the cluster is dominated by a massive cD galaxy, NGC 6166 (Kelson et al. 2002), and the cluster hosts a cooling flow (Johnstone et al. 2002).

Section 2 describes the observational data we use. We construct total IR (TIR; 8–1000 μm) and 12 μm LFs for several subsamples in Section 3. We discuss the results and conclude in Sections 4 and 5, respectively. Throughout we adopt, unless explicitly mentioned otherwise, flat ΛCDM cosmological parameters of $H_0 = 100\,h$ km s^{-1} Mpc^{-1}, $\Omega_\Lambda = 0.7$, and $\Omega_m = 0.3$. One arcmin corresponds to $\sim$26.2 h^{-1} kpc at the redshift of A2199.

2. THE DATA

2.1. Galaxy Catalog

We first constructed a master catalog containing a photometric sample of galaxies with $m_r < 20.11$ (down to the magnitude where the spectroscopic samples exist) in the SDSS data release 7 (DR7; Abazajian et al. 2009). We selected galaxies within 6.°7 ($\sim$10 h^{-1} Mpc) of the A2199 center ($\alpha = 16^{\rm h}28^{\rm m}38^{\rm s}$, $\delta = +39^\circ32'55''$; Böhringer et al. 2000).

Spectroscopic data for galaxies with $m_r < 17.77$ are available in the SDSS database. However, the spectroscopic completeness of the SDSS data is poor for bright galaxies with $m_r < 14.5$ and for galaxies in high-density regions. Thus, we supplement the galaxy data to reduce the effects of incompleteness. We compiled redshifts for the photometric sample of galaxies in the master catalog from the literature (see Hwang et al. 2010 for details). We also included the data from extensive spectroscopic survey programs in the field of A2199 (Rines et al. 2002; Rines & Geller 2008) which include galaxies fainter than the SDSS limit.

Figure 1 shows the spectroscopic completeness of the galaxy sample as a function of apparent magnitude and of clustercentric radius. The spectroscopic completeness of our sample brighter than the SDSS limit is $\gtrsim$90% at all magnitudes and clustercentric radii. Galaxies fainter than the SDSS limit are not completely covered by the spectroscopic observations, but there are useful data within the virial radius of A2199 ($r_{200,\rm A2199}$; to be defined in Section 2.4).

We also use several value-added galaxy catalogs (VAGCs) drawn from SDSS data. We adopt the photometric parameters from the SDSS pipeline (Stoughton et al. 2002). We take the spectroscopic parameters including SFRs (Brinchmann et al. 2004) and oxygen abundance (Tremonti et al. 2004) from the MPA/JHU DR7 VAGC.[5]

We adopt galaxy morphology data from the Korea Institute for Advanced Study (KIAS) DR7 VAGC[6] (Choi et al. 2010). In this catalog, galaxies are divided into early (ellipticals and lenticulars) and late (spirals and irregulars) morphological types

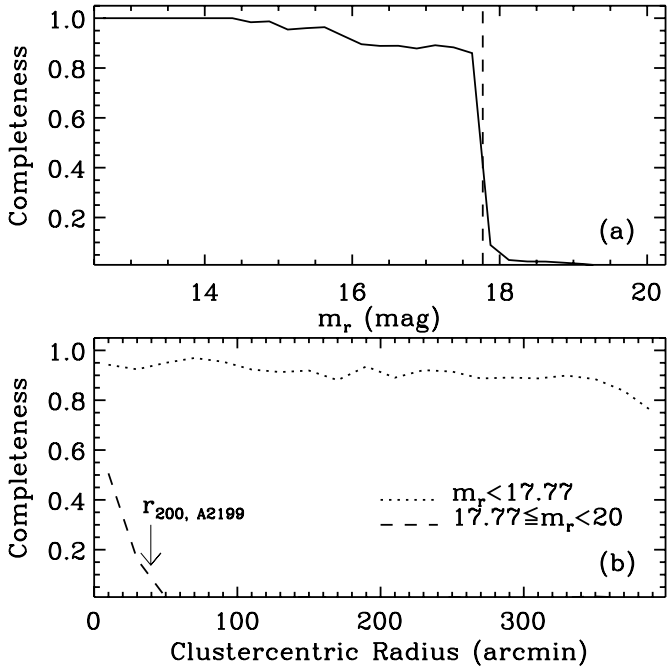

Figure 1. Spectroscopic completeness of our galaxy catalog in the field of A2199 as a function of r-band magnitude (a) and clustercentric radius (b). Vertical dashed line indicates the SDSS limit of the main galaxy sample (i.e., $m_r < 17.77$). The dotted line in (b) is the completeness for galaxies brighter than this limit. The dashed line is for those fainter than the limit. An arrow indicates r_{200} of A2199.

based on their locations in the $(u-r)$ color versus $(g-i)$ color gradient space and in the i-band concentration index space (Park & Choi 2005). The resulting morphological classification has completeness and reliability reaching 90%. We performed an additional visual check of the color images of the galaxies misclassified by the automated scheme, and of the galaxies that are not included in the KIAS DR7 VAGC. In this procedure, we revised the types of blended or merging galaxies, blue but elliptical-shaped galaxies, and dusty edge-on spirals.

2.2. WISE

We use the new wide-field MIR data obtained by the *WISE* satellite, which covers all the sky at four MIR bands (3.4, 4.6, 12, and 22 μm). The *WISE* all-sky source catalog[7] contains photometric data for over 563 million objects. *WISE* covers the entire region of the A2199 supercluster to a homogeneous depth and detects galaxies in this supercluster down to $L_{\rm IR} \sim 10^9\,L_\odot$.

We identified *WISE* counterparts of the galaxies in our master catalog by cross-correlating them with the sources in the *WISE* all-sky data release with a matching tolerance of 3″($\sim$0.5×FWHM of the PSF at 3.4 μm). We use the point source profile-fitting magnitudes, and restrict our analysis to the sources with S/N $\geqslant$ 3 at each *WISE* band. *WISE* 5σ photometric sensitivity is estimated to be better than 0.08, 0.11, 1, and 6 mJy at 3.4, 4.6, 12, and 22 μm in unconfused regions on the ecliptic plane (Wright et al. 2010).

Because 22 μm *WISE* data are closer to the peak of IR emission than other bands and because they are less affected by polycyclic aromatic hydrocarbon (PAH) emission features, we computed the TIR luminosity ($L_{\rm IR}$) from the 22 μm flux density using the spectral energy distribution (SED) templates

[5] http://www.mpa-garching.mpg.de/SDSS/DR7/
[6] http://astro.kias.re.kr/vagc/dr7/
[7] http://wise2.ipac.caltech.edu/docs/release/allsky/

of Chary & Elbaz (2001, hereafter CE01). CE01 contain 105 SED templates with different TIR luminosities ($3 \times 10^8\,L_\odot < L_{\rm IR} < 6 \times 10^{13}\,L_\odot$). The templates provide νL_ν ($L_\odot$) as a function of wavelength. For the observed 22 μm flux density, we choose the closest template to obtain the appropriate TIR luminosity. We interpolate between the two closest templates to reach the observed 22 μm flux density. TIR luminosities extrapolated from a single passband have been examined in many papers. They agree very well with those based on all far-IR (FIR) bands; the uncertainty is ~40% (e.g., Elbaz et al. 2010, 2011). Therefore, this procedure does not introduce any bias in our results. We reexamine it in Section 2.5.1.

2.3. Completeness

To construct IR LFs for galaxies in the supercluster (Section 3), it is necessary to correct for the spectroscopic and photometric incompleteness of our sample. We first compute the spectroscopic completeness of *WISE*-detected sources in the supercluster. At the end of this section we determine the photometric completeness. Because we are only interested in the sources in the supercluster, we compute the spectroscopic completeness for supercluster galaxies. To do that, we select tentative member galaxies from the photometric sample based on the photometric redshift (photo-z), and compute the spectroscopic completeness for these galaxies.

Among several photo-z measurements provided by the SDSS database, we adopt the photometric redshift data based on the Artificial Neural Network technique (Oyaizu et al. 2008). This approach gives the tightest correlation between spectroscopic and photometric redshifts for galaxies at the redshift of A2199 (see also the application to the A1763 supercluster by Biviano et al. 2011). Following Knobel et al. (2009) and Biviano et al. (2011), we determine the optimal photometric redshift range for selecting tentative member galaxies by minimizing $\sqrt{(1-P)^2+(1-C)^2}$. P is the purity of the sample, defined by the ratio of the number of spectroscopically confirmed member galaxies in the optimal photometric redshift range to the number of galaxies with any spectroscopic redshifts in the optimal photometric redshift range. C is the completeness of the sample, the ratio of the number of spectroscopically confirmed member galaxies in the optimal photometric redshift range to the number of spectroscopically confirmed member galaxies with any photometric redshifts. From a simple experiment adjusting the redshift range, we found the optimal photometric redshift range for tentative members: $0.0089 < z_p < 0.0599$.

Using these photo-z selected member galaxies, we compute the spectroscopic completeness for the *WISE*-detected sources at 22 μm and 12 μm, and show the results in Figures 2(a) and (b). Red solid lines are based on all the spectroscopic sample of galaxies compiled in the master catalog. There are many galaxies fainter than the SDSS limit (i.e., $m_{\rm r} \gtrsim -17$) only in the central region ($R \lesssim 30'$), but not in the outer region (see Figure 3(b)). To check any bias introduced by the variation in the depth of the spectroscopic catalog with clustercentric radius, we also plot the spectroscopic completeness based only on the galaxies brighter than the SDSS limit (i.e., $m_r < 17.77$) as blue solid lines. Because the two curves are very similar, the LFs based on these two curves should not differ significantly (see Section 3).

We take the photometric completeness for *WISE* sources from the Explanatory Supplement to the *WISE* all-sky data release products, which gives completeness curves for several (16–80, the effective number of times that point on the sky

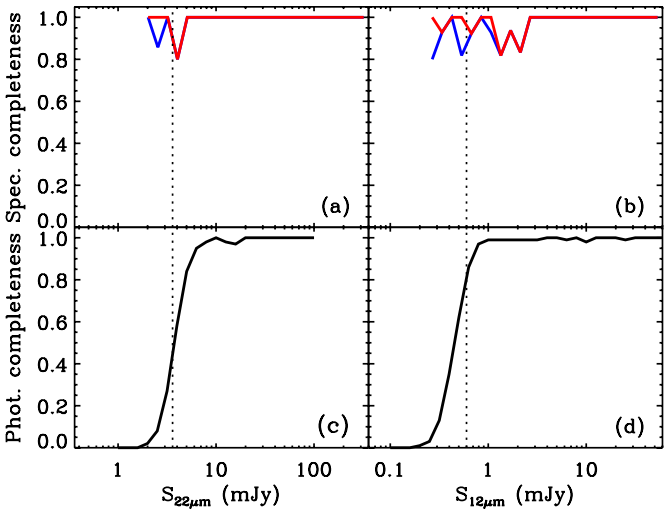

Figure 2. (Top) Spectroscopic completeness of *WISE*-detected (>3σ) galaxies with $0.0089 < z_{\rm phot} < 0.0599$ at 22 μm (left) and at 12 μm (right). Blue and red curves are the completeness computed for the galaxies brighter than the SDSS limit and for all the galaxies including those fainter than the limit, respectively. (Bottom) *WISE* photometric completeness for the A2199 supercluster region with a mean coverage depth of ~21 at 22 μm (left) and 12 μm (right). Vertical dashed lines indicate 3σ flux limits (3.6 and 0.6 mJy for 22 and 12 μm, respectively).

(A color version of this figure is available in the online journal.)

was visited by a "good" detector frame pixel[8]) coverage depth.[9] By interpolating the curves in the Explanatory Supplement, we show the photometric completeness curves at 22 μm and 12 μm for the A2199 supercluster region with a coverage depth of ~21 (Figures 2(c) and (d)).

When we compute the IR LFs using *WISE*-detected galaxies, we weight each galaxy by the inverse of the photometric and spectroscopic completeness as a function of *WISE* flux density.

2.4. Supercluster Membership

To determine the membership of galaxies in the A2199 supercluster, we used the caustic method (Diaferio & Geller 1997; Diaferio 1999; Serra et al. 2011). The technique locates two curves, the caustics, in the cluster redshift diagram (Figure 3(a)) that shows the line-of-sight velocities of galaxies as a function of distance from the center of the supercluster.

The caustics measure the escape velocity from the system of galaxies and provide a basis for measurement of the mass of the system (Rines et al. 2002). The caustics are also a useful tool for defining supercluster membership. Samples identified with the caustic technique are at least 95% complete. At most 10% of the galaxies projected within the caustics are interlopers. Most of these are well within the caustics (i.e., they are not velocity outliers; Serra et al. 2010; A. L. Serra et al., in preparation).

We applied the technique to a sample of 11,478 spectroscopic redshifts in the field of the A2199 supercluster. The technique identifies 1736 members within ~10 h^{-1} Mpc of the supercluster center. Among these, 550 and 1155 galaxies are detected (>3σ) at *WISE* 22 μm and 12 μm, respectively. The cluster center determined from this technique is consistent with the X-ray center used in this study (see Appendix A of Diaferio 1999 for more details). Table 1 summarizes the statistics for the number of galaxies in our sample.

[8] The exposure time for a single visit corresponds to 7.7 s (3.4 and 4.6 μm) and 8.8 s (12 and 22 μm).

[9] http://wise2.ipac.caltech.edu/docs/release/allsky/expsup/sec6_5.html

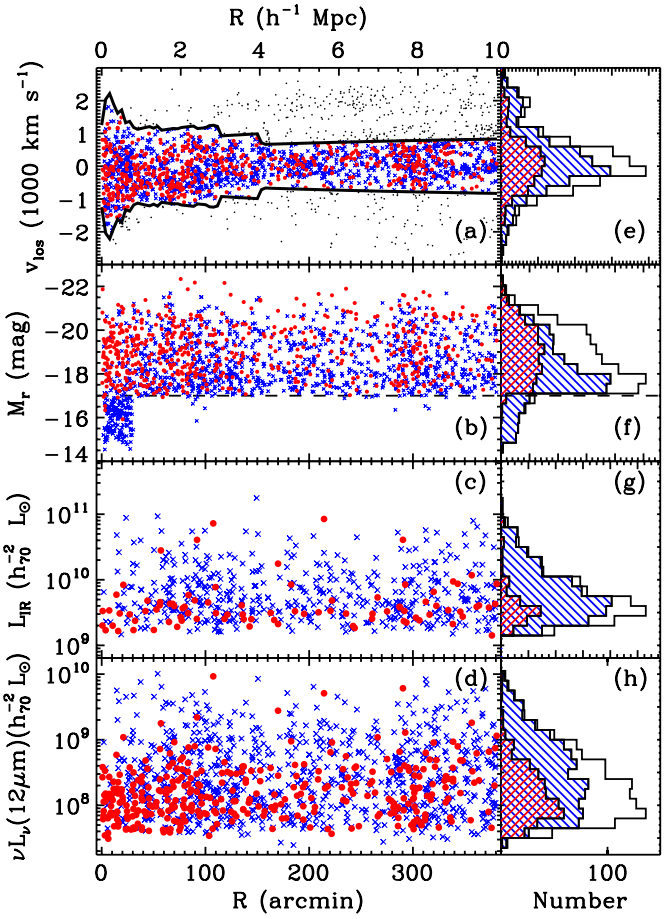

Figure 3. Line-of-sight velocity relative to the cluster (a), *r*-band absolute magnitude (b), TIR luminosity (c), and 12 μm luminosity (d) as a function of clustercentric radius, and their histograms (e–h). We use the mean cluster redshift, $cz = 9370$ km s^{-1}, determined from the caustic method. Red filled circles and blue crosses indicate early- and late-type member galaxies, respectively. Black dots indicate non-member galaxies. The thick solid line indicates the estimated location of the caustics. Open histogram show the total sample, and early- and late-type galaxies are denoted by hatched histograms with orientation of 45° (// with red colors) and of 315° (\\ with blue colors), respectively. The horizontal dashed lines in (b) and (f) indicate the SDSS magnitude limit.

(A color version of this figure is available in the online journal.)

In Figure 3, we plot several physical parameters of the member galaxies as a function of clustercentric radius and morphology. Thanks to the deep spectroscopic survey in Rines & Geller (2008), many faint galaxies with $m_r > -17$ at $R < 30'$ are included as members (b). Few luminous infrared galaxies (LIRGs, $L_{IR} > 10^{11}$ $L_\odot$) reside in this supercluster (c), consistent with expectation ($\lesssim$1 LIRGs in the supercluster volume) from the field IR luminosity density at this epoch (Goto et al. 2011b).

Figure 4 shows the spatial distribution of the member galaxies segregated by their morphologies. The galaxy number density map constructed using the member galaxies with $m_r \leqslant 17.77$ mag and the X-ray intensity contours from *ROSAT* All-Sky Survey are overlaid.

The galaxy density peaks match several known galaxy groups with X-ray emission shown by blue dashed circles (Rines et al. 2001, 2002). The radius of the circle indicates r_{200} of each group (approximately the virial radius). Within this radius, the mean overdensity is 200 times the critical density of the universe ρ_c. We compute r_{200} from the formula given by Carlberg et al. (1997):

$$r_{200} = \frac{3^{1/2}\sigma_{cl}}{10H(z)}, \quad (1)$$

where σ_{cl} is the velocity dispersion of the cluster from Rines et al. (2002), and the Hubble parameter at z is $H^2(z) = H_0^2[\Omega_m(1+z)^3 + \Omega_k(1+z)^2 + \Omega_\Lambda]$ (Peebles 1993). Ω_m, Ω_k, and Ω_Λ are the dimensionless density parameters. Because the observed velocity dispersions of the groups in the infall region could be increased by the supercluster dynamics (e.g., see Table 8 in Rines et al. 2002), the r_{200} of each group shown in Figure 4 should be considered only as a rough estimate of the group size.

Table 1
Number of Galaxies in the A2199 Supercluster

Wavelength	Early Types		Late Types		Total
(μm)	AGN	Non-AGN	AGN	Non-AGN	
Spectroscopic Sample of Galaxies at $R < 380$ arcmin					
All	334	4322	1242	5580	11478
3.4	332	4259	1237	5381	11209
4.6	332	4259	1231	5346	11168
12	289	2130	1198	4741	8358
22	118	271	892	2403	3684
Member Galaxies at $R < 380$ arcmin					
All	39	531	135	1031	1736
3.4	39	522	135	948	1644
4.6	39	522	131	922	1614
12	37	309	116	693	1155
22	16	70	92	372	550

2.5. Comparison between WISE and SDSS data

2.5.1. Star Formation Rate

Because we have SFR_{WISE} from the *WISE* 22 μm flux density and SFR_{SDSS} measured from the SDSS optical spectra, the comparison between the two measurements is an important sanity check for the new *WISE* data (see also Donoso et al. 2012). Among 1736 member galaxies in the A2199 supercluster, there are 1468 and 550 galaxies with SFR_{SDSS} and SFR_{WISE}, respectively.

The SFR_{SDSS} is from the MPA/JHU DR7 VAGC (Brinchmann et al. 2004), which provides extinction and aperture corrected SFR estimates of star-forming galaxies as well as other types of galaxies (e.g., AGN, composite, low-S/N SF, low-S/N LINER, and unclassifiable). They correct the extinction following the dust treatment of Charlot & Fall (2000), which compares the observed line ratios with those expected from models with different dust attenuations. For those galaxies where they cannot directly measure SFRs from the emission lines such as active galactic nuclei (AGNs) and composite galaxies, they use the 4000 Å break (D4000) to estimate SFRs (see Brinchmann et al. 2004 and http://www.mpa-garching.mpg.de/SDSS/DR7/sfrs.html for more details). SFR_{WISE} is converted from the TIR luminosity using the relation in Kennicutt (1998) with the assumption of a Salpeter IMF (Salpeter 1955): SFR_{WISE} ($M_\odot$ yr^{-1}) = $1.72 \times 10^{-10} L_{IR}(L_\odot)$.

We show the comparison between SFR_{SDSS} and SFR_{WISE} in Figure 5 based only on the galaxies with star-forming spectral type (see Section 2.5.2). The figure shows that SFR_{WISE} agrees well with SFR_{SDSS}, demonstrating consistency between the two measurements.

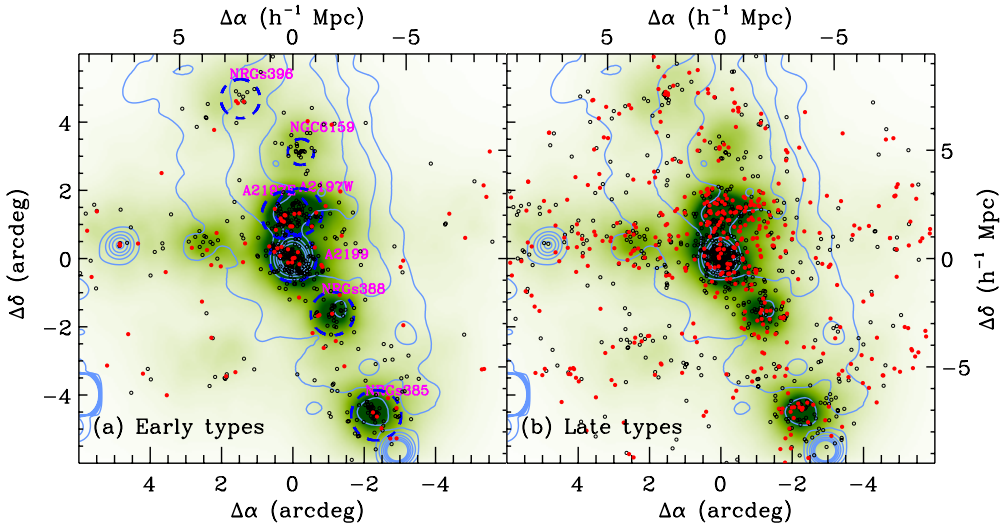

Figure 4. Spatial distribution of early-type (left) and late-type (right) galaxies in the A2199 supercluster overlaid on the green and white total galaxy number density maps. Contours with sky-blue color indicate the X-ray intensity map taken from the *ROSAT* All-Sky Survey, smoothed with a Gaussian filter of $\sigma = 15$ arcmin. Galaxies with and without *WISE* 22 μm detections are denoted by red, filled and black, open symbols, respectively. Dashed circles in (a) represent r_{200} of galaxy groups in the A2199 supercluster (Rines et al. 2001, 2002). North is up, and east is to the left.

(A color version of this figure is available in the online journal.)

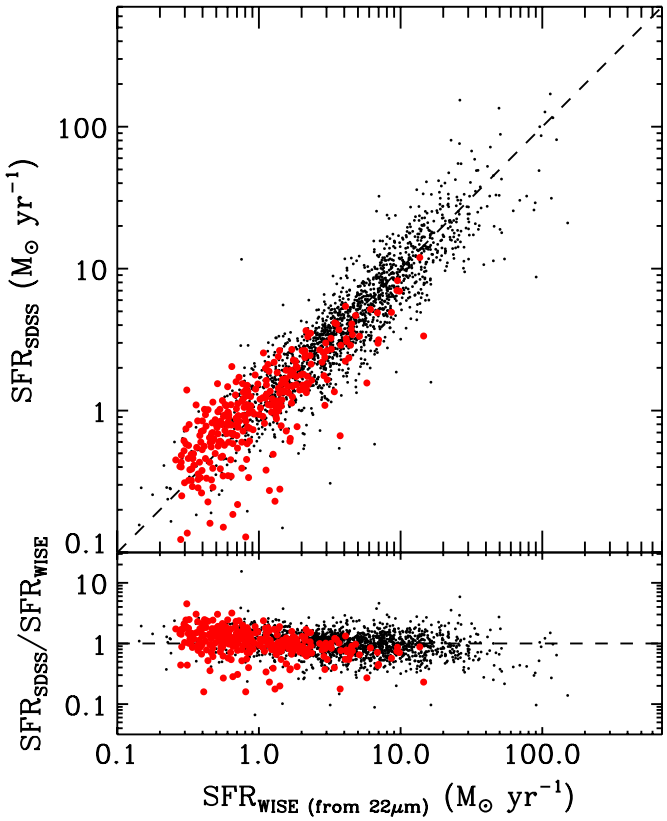

Figure 5. Comparison of SFRs from *WISE* 22 μm flux density (SFR_{WISE}) with those from SDSS spectra (SFR_{SDSS}) We plot only galaxies with star-forming spectral type (SF, see Section 2.5.2). Large, red circles are for member galaxies in the A2199 supercluster, and small, black dots are for all the galaxies at $z < 0.22$ in the field of A2199.

(A color version of this figure is available in the online journal.)

2.5.2. AGN Selection

We determined the spectral types of emission-line galaxies using the criteria of Kewley et al. (2006) based on the Baldwin–Phillips–Terlevich (BPT) emission-line ratio diagrams (Baldwin et al. 1981; Veilleux & Osterbrock 1987). For galaxies with signal-to-noise ratio (S/N) $\geqslant 3$ in the strong emission lines Hβ, [O III] λ5007, Hα, [N II] λ6584, and [S II] $\lambda\lambda$6717,6731, we determined the spectral types based on their positions in the line ratio diagrams with [O III]/Hβ plotted against [N II]/Hα, [S II]/Hα, and [O I]/Hα. These types are star-forming galaxies, Seyferts, low-ionization nuclear emission-line regions (LINERs), composite galaxies, and ambiguous galaxies (see Kewley et al. 2006 for more details).

Composite galaxies host a mixture of star formation and AGN, and lie between the extreme starburst line (Kewley et al. 2001) and the pure star formation line (Kauffmann et al. 2003) in the [O III]/Hβ versus [N II]/Hα line ratio diagram (see Figure 6(a)). Ambiguous galaxies are those classified as one type in one or two diagrams, but as another type in the other diagrams (see Kewley et al. 2006 for more details). We assign "undetermined" type to those that do not satisfy the S/N criteria.

These AGN criteria select only Type II AGNs with narrow emission lines, and miss Type I AGNs with broad Balmer lines. To identify Type I AGNs missed in this method, we included galaxies with a quasar spectral classifications provided by the SDSS pipeline (i.e., `specClass` = `SPEC_QSO` or `SPEC_HIZ_QSO`; see Stoughton et al. 2002 for more details). Among 1736 member galaxies, three galaxies are Type I AGNs.

There could be still unidentified AGNs in our sample. There are some galaxies without an SDSS spectrum because their redshifts are from the literature. In some galaxies, the AGN signature may be hidden by dust (e.g., Lee et al. 2011). To identify additional AGNs, we plot *WISE* color–color diagrams in Figures 6(b) and (c). Interestingly, the main locus of optically selected AGN-host galaxies is not clearly distinguishable from the loci of other non-AGN galaxies. If the dust is heated by AGNs, the [3.4]–[4.6] color should be red (see Assef et al. 2010). Therefore, we use the criterion [3.4]–[4.6] > 0.44 (Vega) to select AGNs at the redshift of A2199. Among eight galaxies satisfying this criterion with known spectral types, six are AGN-host galaxies. This criterion is slightly bluer than the AGN

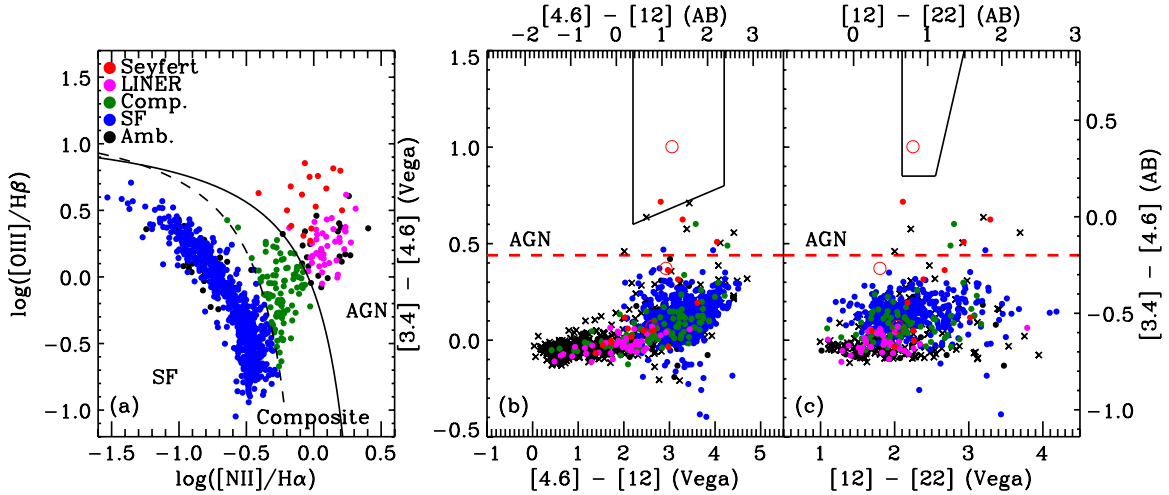

Figure 6. AGN diagnostic diagrams for the member galaxies in the A2199 supercluster based on (a) optical [O III]/Hβ vs. [N II]/Hα line ratios; (b) and (c) *WISE* colors. Different spectral types following the scheme of Kewley et al. (2006) are represented by different colored symbols (Seyfert: red; LINER: pink; composite: green; SF: blue; ambiguous: black). The solid and dashed lines indicate the extreme starburst (Kewley et al. 2001) and pure SF limits (Kauffmann et al. 2003), respectively. Open red circles in (b) and (c) are Type I AGNs, and crosses in (b) and (c) are those whose spectral types are not determined because of lack of optical spectra. Solid lines in (b) and (c) are the AGN selection criteria proposed by Jarrett et al. (2011) and Assef et al. (2010), respectively. Horizontal dashed lines in (b) and (c) are the AGN selection criteria used in this study for galaxies in the A2199 supercluster.

(A color version of this figure is available in the online journal.)

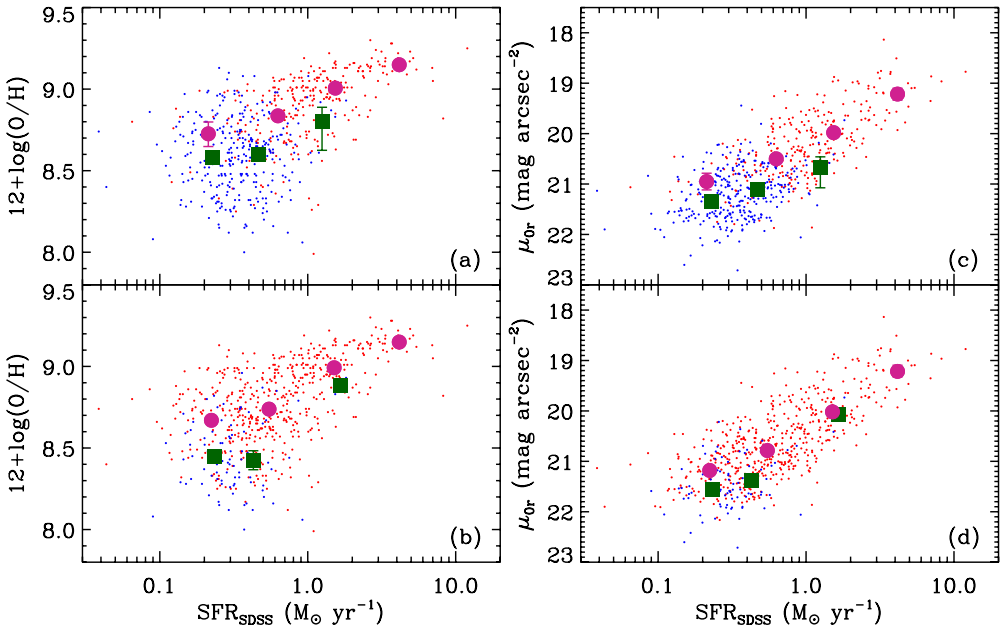

Figure 7. (Left) Oxygen abundance and (right) *r*-band surface brightness of *WISE*-detected ($>3\sigma$) galaxies (red) and undetected ($<3\sigma$) galaxies (blue) at 22 μm (top) and 12 μm (bottom). We only plot the member galaxies in the A2199 supercluster. Large purple circles (with *WISE* detection) and green squares (without *WISE* detection) are median values of each physical parameter and of $\mathrm{SFR_{SDSS}}$ at each bin. The error bars represent 68% (1σ) confidence intervals determined by the bootstrap resampling method.

(A color version of this figure is available in the online journal.)

selection criteria used in Assef et al. (2010) and Jarrett et al. (2011), but is similar to the one in Chung et al. (2011). In summary, we classify AGN-host galaxies as objects with either a Type I or Type II (Seyferts, LINERs, and composites) AGN optical spectrum, and we classify MIR AGNs from the *WISE* color–color diagram.

2.5.3. Metallicity and Surface Brightness

To understand possible systematics in the samples of *WISE*-detected and undetected galaxies, we plot the oxygen abundance [12+log(O/H)] and the central surface brightness of the member galaxies in the A2199 supercluster as a function of SFR in Figure 7. Following Rines & Geller (2008), we compute the central surface brightness (in units of mag arcsec^{-2}) from the SDSS fiber magnitudes using the equation $\mu_{0r} = m_{r,\mathrm{fiber}} + 2.123$ assuming constant surface brightness within the fiber.

Because of increasing dust obscuration (also increasing dust-to-gas ratio) with gas-phase metallicity (e.g., Heckman et al. 1998; Leroy et al. 2011; Magdis et al. 2011), *WISE*-detected galaxies that have IR emission from dust should be more metal-rich than undetected galaxies. If we focus on a range 0.1 $M_\odot$ yr^{-1} $<$ $\mathrm{SFR_{SDSS}}$ $<$ 1 $M_\odot$ yr^{-1} where both

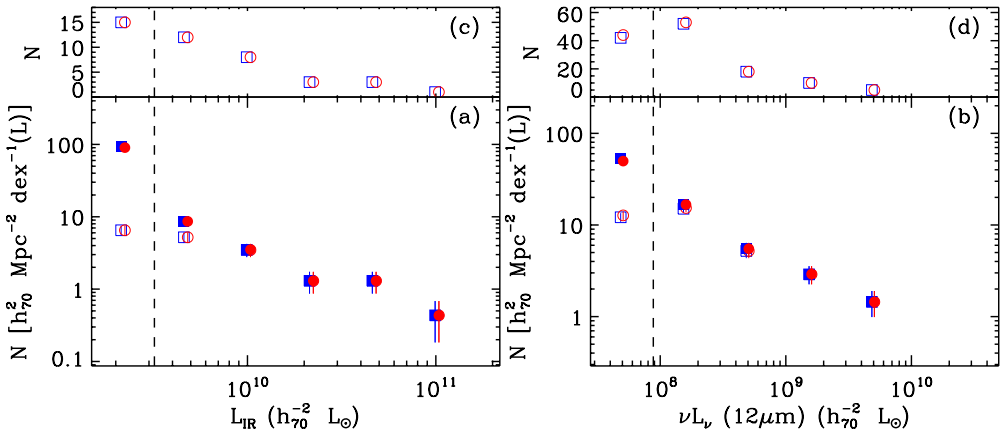

Figure 8. (Bottom) TIR (a) and 12 μm (b) LFs for galaxies in the central region of the rich cluster A2199 (i.e., $R < r_{200,A2199} \approx 40'$). Squares are the LFs based on the galaxies brighter than the SDSS limit. Circles include all the galaxies fainter than the limit. Open symbols are the raw LFs, and filled symbols are those after the corrections for photometric and spectroscopic incompleteness. The associated error bars indicate Poisson uncertainties. Vertical dashed lines indicate the luminosity limits at the redshift of A2199 corresponding to 3σ flux limits (3.6 mJy and 0.6 mJy for 22 μm and 12 μm, respectively). (Top) Number of galaxies used for the construction of the LFs in each bin for TIR (c) and 12 μm (d). Circles in the left panels are not shown because there are no 22 μm detections for galaxies fainter than the SDSS limit.

(A color version of this figure is available in the online journal.)

WISE-detected and undetected galaxies exist, we can clearly see at both 22 and 12 μm that the oxygen abundance of *WISE*-detected galaxies is always higher than that of undetected galaxies. Similarly, the right panels show that *WISE*-detected galaxies tend to have higher surface brightness than undetected galaxies at a fixed SFR. Because the metallicity and the surface brightness are strongly coupled (Ryder 1995; Simon et al. 2006), it is difficult to conclude which is a more fundamental parameter. In any case, we conclude that MIR-detected galaxies tend to be more metal-rich and to have higher surface brightness than those without an MIR detection. If we use all the galaxies in the redshift range of the A2199 supercluster regardless of supercluster membership, the results do not change. Thus, these results are not biased by the supercluster environment.

3. LUMINOSITY FUNCTIONS

Here we compute the projected TIR and 12 μm LFs for galaxies in the A2199 supercluster. Because the depth of the spectroscopic survey is not the same in the central region of A2199 and in the outer regions (see Figure 3(b)), we first start with the LFs in the central region to check for bias introduced by the variation in the depth of the spectroscopic survey as a function of clustercentric radius. We construct the LFs by first counting the number of member galaxies. We then divide by the survey area in physical size and by the bin size $\Delta(\log L)$. Then we correct the counts for spectroscopic and photometric incompleteness by weighting each galaxy with the inverse of each completeness as a function of its *WISE* flux density (Section 2.2).

Figure 8 shows TIR and 12 μm LFs for galaxies in the central cluster A2199 (i.e., $R \lesssim r_{200,A2199} \approx 40'$). Open squares show the raw LFs without the completeness correction using the galaxies brighter than the SDSS limit. The filled squares indicate the corrected LFs. As expected, the correction only affects the faint end of the LFs.

To check the effect of the galaxies fainter than the SDSS limit on the derived LFs, we recompute the LFs again including these galaxies. We show the results in the figure with circle symbols (open for raw LFs and filled for corrected LFs). The two corrected LFs based on bright (squares) and total (circles) samples agree well. The TIR LF (left panel) based on the total sample is not shown because there are no 22 μm detected galaxies fainter than the SDSS limit in this central cluster A2199. The agreement between the two corrected LFs occurs mainly because the spectroscopic completeness for the *WISE* sources in this supercluster region is high even when we restrict our analysis to galaxies brighter than the SDSS limit (see Figure 2). This result suggests that the corrected LFs based only on the bright sample are robust. Because the entire region of the supercluster is covered uniformly by the SDSS data, we restrict the following analysis to the galaxies brighter than the SDSS limit for consistency.

3.1. LFs for Subsamples

We next explore TIR and 12 μm LFs for galaxies in the A2199 supercluster as a whole (Figure 9). We fit the LFs with a classical Schechter (1976) function:

$$\phi(L) = \frac{dN(L)}{dA\, d\log(L)} = \phi^\star \left(\frac{L}{L^\star}\right)^{1+\alpha} \exp\left(-\frac{L}{L^\star}\right). \quad (2)$$

We fit the data above the 3σ flux limit (3.6 mJy and 0.6 mJy for 22 μm and 12 μm, respectively), shown as a vertical dashed line in each panel. We use the MPFIT package in IDL (Markwardt 2009, an implementation of the Levenberg–Marquardt minimization), and compute the uncertainty of the faint-end slope by repeating the fitting procedure 1000 times for random perturbations of the fitted data points within their errors (following a normal distribution).

Because the bright end of the LFs is not well constrained due to the small number of IR bright galaxies in this supercluster, we focus mainly on the faint-end slope of the LFs. The faint-end slope of the TIR LF for the total sample is $\alpha = -2.14 \pm 0.06$. The slope of the TIR LF for AGN-host galaxies is $\alpha = -1.64 \pm 0.13$, shallower than that for non-AGN galaxies ($\alpha = -2.36 \pm 0.05$), indicating an increasing contribution of AGN-host galaxies to the TIR LFs with increasing IR luminosity as seen in previous studies (e.g., Goto et al. 2011a, 2011b). Because the slopes of the LFs do not seem to change with TIR luminosity,

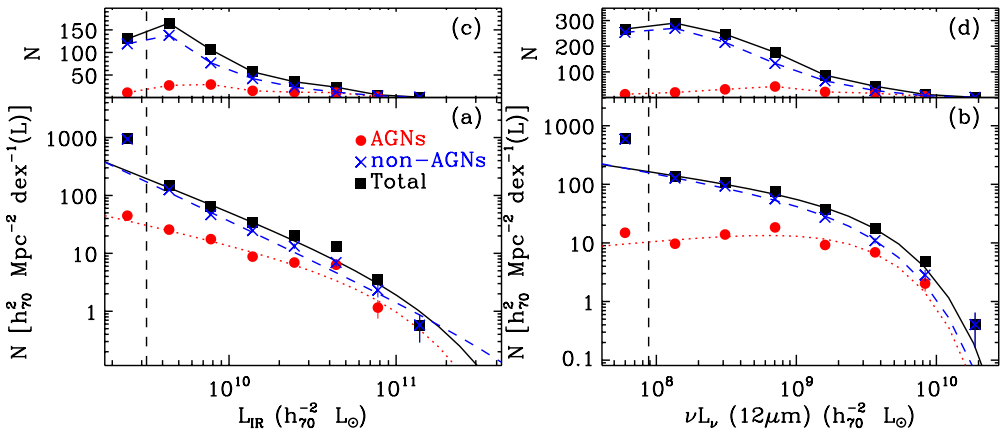

Figure 9. (Bottom) TIR (a) and 12 μm (b) LFs for galaxies in the entire supercluster region (i.e., $R < 380'$). Circles and crosses are for AGN-host and non-AGN galaxies, respectively, and squares are for the total sample. Dotted and dashed lines are the best-fit Schechter functions for AGN-host and non-AGN galaxies, respectively, and solid line is for the total sample. Vertical dashed lines indicate the luminosity limits at the redshift of A2199 corresponding to 3σ flux limits (3.6 and 0.6 mJy for 22 and 12 μm, respectively). (Top) Number of galaxies used for the construction of the LFs in each bin for TIR (c) and 12 μm (d).

(A color version of this figure is available in the online journal.)

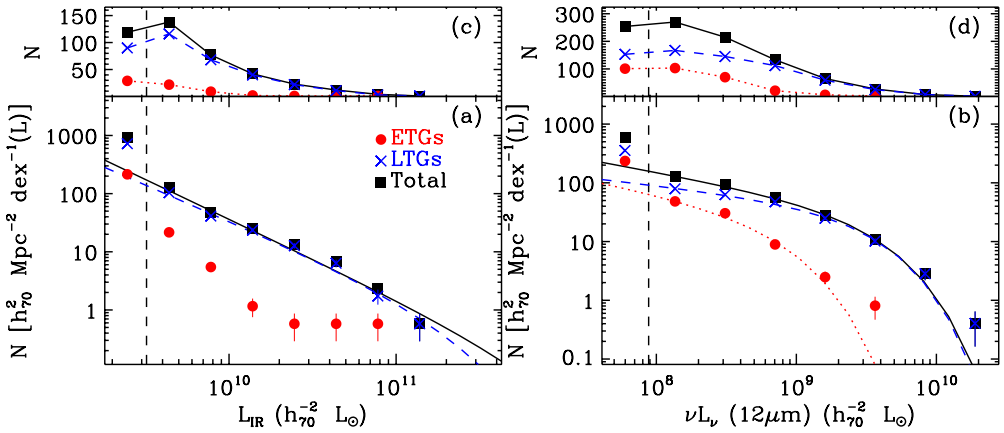

Figure 10. Same as Figure 9, but for early-type (ETGs; circles and dotted lines) and late-type galaxies (LTGs; crosses and dashed lines) after rejecting AGN-host galaxies.

(A color version of this figure is available in the online journal.)

we also fit the LFs with a power-law function (see also Biviano et al. 2011 for the case of the A1763 supercluster). We obtain similar values of $\alpha = -2.19 \pm 0.03$, -1.76 ± 0.05, and -2.35 ± 0.04 for the total sample, AGN-host and non-AGN galaxies, respectively.

The faint-end slope for non-AGN galaxies (i.e., SF galaxies) is steeper than the slope based on *IRAS* photometry ($\alpha = -0.6$) for the *IRAS* revised bright galaxy sample (RBGS; Sanders et al. 2003) and the slope ($\alpha \approx -1.41$) found for cluster galaxies (Bai et al. 2006, 2009; Haines et al. 2011). The steeper slope probably results partly from the very high spectroscopic completeness in this study. However, it is only slightly steeper than the slope based on recent *AKARI* photometry for RBGS ($\alpha = -1.9 \pm 0.1$ and -1.8 ± 0.1 for SF galaxies and for the total sample, respectively; Goto et al. 2011a) and the slope for the *AKARI*-detected SDSS galaxies ($\alpha = -1.8 \pm 0.1$ and -1.99 ± 0.09 for SF galaxies and total sample, respectively; Goto et al. 2011b). In addition, it is broadly consistent with the faint-end slopes based on all the galaxies in the A1763 supercluster (Biviano et al. 2011).

In Figure 9(b), the AGN contribution again increases with 12 μm luminosity (Spinoglio & Malkan 1989). The faint-end slope is $\alpha = -1.35 \pm 0.03$ and -1.44 ± 0.04 for the total sample and for the non-AGN galaxies, respectively. These slopes are consistent with those based on *IRAS* galaxy samples (Fang et al. 1998) and those based on the local sample of *Spitzer*-detected galaxies (Pérez-González et al. 2005).

When we decompose the LFs based on galaxy morphology by rejecting AGN-host galaxies (see Figure 10), the contribution of early-type galaxies to the TIR LFs is very small as expected (left panels). The faint-end slope for late-type galaxies in TIR LFs is $\alpha = -2.23 \pm 0.07$, again consistent with the slope from the power-law function ($\alpha = -2.28 \pm 0.04$). For the 12 μm LFs, the faint-end slopes are $\alpha = -1.48 \pm 0.30$ and $\alpha = -1.27 \pm 0.05$ for early- and late-type galaxies, respectively, suggesting that the contribution of early-type galaxies increases with decreasing luminosity (see the right panel of Figure 10 and Section 4.2). We list the faint-end slopes for several subsamples in Table 2.

3.2. Environmental Dependence of LFs

3.2.1. TIR LFs: No Environmental Dependence

To study the environmental dependence of the LFs, we divide the galaxies into three radial ranges $R \leqslant 98' \approx 2.6\ h^{-1}$ Mpc, $98' < R \leqslant 249'$, and $R > 249' \approx 6.5\ h^{-1}$ Mpc so that each range contains a similar number of galaxies. Then we plot TIR LFs for galaxies only in the inner and outer regions (to emphasize the difference if any) in Figure 11. We reject

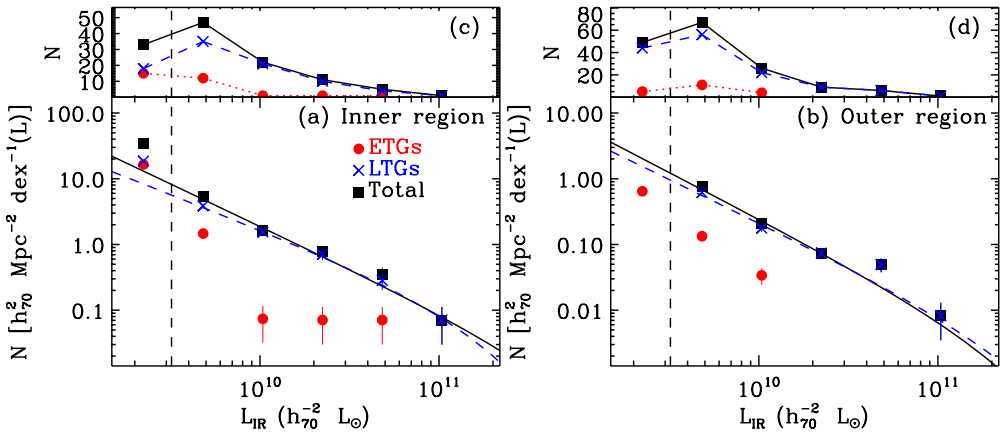

Figure 11. TIR LFs for galaxies after rejecting AGN-host galaxies in the inner ($R \leqslant 98' \approx 2.6\ h^{-1}$ Mpc) region (a) and in the outer ($R > 249' \approx 6.5\ h^{-1}$ Mpc) region (b). Circles and crosses are for early- and late-type galaxies, respectively, and squares are for the total sample. To sense the change of the slope of the LFs if any, we match the scales of the *Y*-axis of the two panels.

(A color version of this figure is available in the online journal.)

Table 2
Faint-end Slopes of IR LFs in the A2199 Supercluster

Sample[a]	Total[b]	AGNs	Non-AGNs	ETGs	LTGs
TIR LFs					
Entire region	-2.14 ± 0.06	-1.64 ± 0.13	-2.36 ± 0.05	...	-2.23 ± 0.07
Inner region	-2.29 ± 0.12	...	...	...	-2.06 ± 0.18
Outer region	-2.41 ± 0.11	...	...	...	-2.31 ± 0.12
12 μm LFs					
Entire region	-1.35 ± 0.03	-0.77 ± 0.08	-1.44 ± 0.04	-1.48 ± 0.30	-1.27 ± 0.05
Inner region	-1.66 ± 0.07	...	...	-2.06 ± 0.25	-1.38 ± 0.08
Outer region	-1.34 ± 0.09	...	...	-1.47 ± 0.31	-1.28 ± 0.10

Notes.
[a] Inner region: $R \leqslant 98' \approx 2.6\ h^{-1}$ Mpc; outer region: $R > 249' \approx 6.5\ h^{-1}$ Mpc.
[b] The faint-end slopes of LFs for the total samples in the inner and outer regions and for ETGs and LTGs are computed after rejecting AGN-host galaxies.

AGN-host galaxies in each sample. The faint-end slope changes from $\alpha = -2.29 \pm 0.12$ (inner region) to $\alpha = -2.41 \pm 0.11$ (outer region) for the total sample, and $\alpha = -2.06 \pm 0.18$ (inner region) to $\alpha = -2.31 \pm 0.12$ (outer region) for late-type galaxies. These results indicate no difference in the faint-end slope. The faint-end slopes of the LFs in the intermediate region are similar.

Consistent with previous studies (Bai et al. 2009; Finn et al. 2010; Haines et al. 2011), our results show that the cluster and field IR LFs do not differ significantly. Biviano et al. (2011) also found similar slopes for three different regions in the A1763 supercluster (i.e., the cluster core, the large-scale filament, and the cluster outskirts). However, they also reported that the filament apparently has a flatter LF than both the outskirts and the core (note that their LFs are complete only down to $L_{IR} = 2.5 \times 10^{10}\ L_{\odot}$). Interestingly, in the Coma cluster, Bai et al. (2006) suggested a hint of a steeper slope toward the outer region of the cluster. Considering the large uncertainty in the determination of the faint-end slope (strongly affected by the spectroscopic and photometric incompleteness), a detailed analysis with a more comprehensive data set of cluster galaxies including Coma is necessary to draw a firm conclusion.

Comparison of our LFs with other LFs based on different SF tracers is also interesting. For example, Cortese et al. (2005, 2008) found a steeper faint-end slope and a brighter $L^{\star}$ in *Galaxy Evolution Explorer* UV LFs for nearby clusters including Virgo, Coma, and A1367 (also for the Shapley supercluster in Haines et al. 2011) than for the field UV LFs. They argued that the steep faint-end slope observed in clusters results from a significant contribution of non-SF galaxies at faint UV magnitudes. If they only consider SF galaxies, the cluster faint-end slope is consistent with the field. Intriguingly, the comparison of Hα LFs between cluster (Coma, A1367, and Virgo) and field galaxies suggests a shallower faint-end slope in clusters than in the field (e.g., Iglesias-Páramo et al. 2002; Shioya et al. 2008; Westra et al. 2010). However, the comparison between the two at high-z ($z \sim 0.8$) suggests similar slopes (Koyama et al. 2010).

3.2.2. 12 μm LFs: Strong Environmental Dependence

Unlike the case of TIR LFs, the change of faint-end slopes in 12 μm LFs with the clustercentric radius in the A2199 supercluster appears significant (see Figure 12): we find $\alpha = -1.66 \pm 0.07$ (inner region) and $\alpha = -1.34 \pm 0.09$ (outer region) for the total sample after rejecting AGN-host galaxies. This change could result from a different morphological mix and/or an intrinsically different slope of the LF with clustercentric radius. Thus, we plot the LFs for early and late types separately in the figure.

The most striking feature in Figure 12 is that the contribution of early types to the faint-end LF is comparable to that of

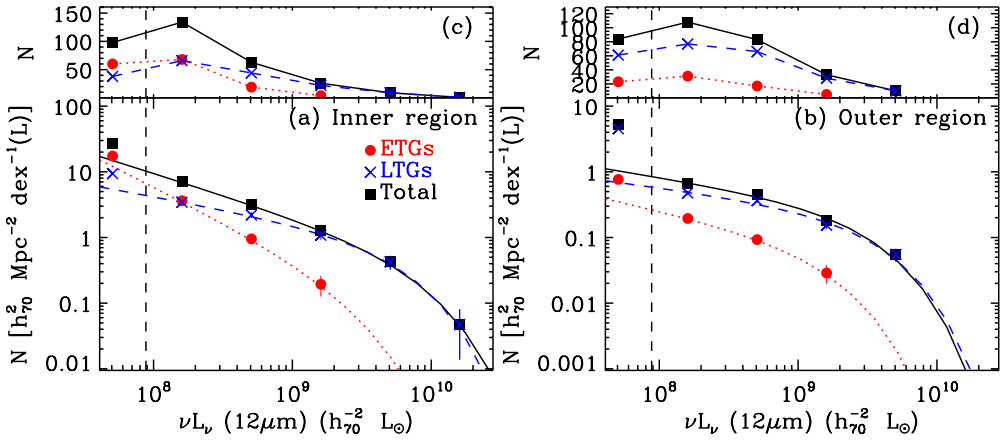

Figure 12. Same as Figure 11, but for 12 μm LFs.
(A color version of this figure is available in the online journal.)

late types in the inner region (a). The faint-end slope of the LFs for early-type galaxies changes from $\alpha = -2.06 \pm 0.25$ (inner region) to $\alpha = -1.47 \pm 0.31$ (outer region), and from $\alpha = -1.38 \pm 0.08$ (inner region) to $\alpha = -1.28 \pm 0.10$ (outer region) for late-type galaxies.

These results suggest that the slope of 12 μm LFs changes with the clustercentric radius only for early-type galaxies, and therefore the change of faint-end slope for the total sample results primarily from the different morphological mix depending on the clustercentric radius (i.e., the increasing contribution of early-type galaxies to the faint end of 12 μm LFs toward the cluster center). If we divide the galaxies based on local density instead of clustercentric radius, the results for both TIR and 12 μm LFs do not change.

4. DISCUSSION

4.1. MIR Star-forming Sequence in the MIR Color–Luminosity Diagram

12μm LFs are very interesting because a variety of mechanisms in galaxies contribute to the SED at this wavelength (Draine & Li 2007): SF driven dust continuum and PAH emission features (Smith et al. 2007; Rieke et al. 2009), hot dust component heated by AGNs (Netzer et al. 2007; Mullaney et al. 2011), and dusty circumstellar envelopes of asymptotic giant branch (AGB) stars (Bressan et al. 1998; Piovan et al. 2003; see also Kelson & Holden 2010).

To investigate the galaxy population responsible for the change of faint-end slopes in the 12 μm LFs with environment, we plot an MIR color–luminosity diagram for the supercluster member galaxies in Figure 13. MIR colors such as *WISE* [3.4]–[22], [4.6]–[12], or *AKARI* [3]–[11] are useful indicators of the specific SFR and of the presence of intermediate-age stellar populations (e.g., Ko et al. 2009, 2012; Shim et al. 2011; Donoso et al. 2012). Figure 13(a) (top panel) clearly shows that there is an "MIR star-forming sequence" of late-type, SF galaxies; there is a very good correlation between [3.4]–[12] and 12 μm luminosity. The sequence here does not extend to LIRGs because they are absent in this A2199 supercluster. The linear fit to the data gives a relation with an rms $\sigma_{[3.4]-[12]} = 0.30$,

$$[3.4]\text{–}[12] = \log(\nu L_\nu(12\,\mu\text{m})) \times (0.64 \pm 0.03) - (4.33 \pm 0.21). \quad (3)$$

The luminosities at 12 μm and at 3.4 μm show strong correlations with SFRs and stellar masses, respectively (Donoso et al. 2012; Li et al. 2007). The SFR is also correlated with stellar mass (Noeske et al. 2007; Elbaz et al. 2007). Thus, the MIR color, [3.4]–[12], can be written as a function of SFR (or stellar mass). Therefore, the color [3.4]–[12] increases with 12 μm luminosity as a result of the underlying correlations.

In Figure 13(b), the distributions of most AGN-host galaxies are distinct from the locus of SF galaxies. Their colors are slightly bluer than the SF sequence and their 12 μm luminosities are relatively high (i.e., $\nu L_\nu(12\,\mu\text{m}) \gtrsim 3 \times 10^8\ h_{70}^{-2}\ L_\odot$). There are some galaxies with "undetermined" spectral types in the faint end of the SF sequence (i.e., $\nu L_\nu(12\,\mu\text{m}) \lesssim 3 \times 10^8\ h_{70}^{-2}\ L_\odot$). They are probably dusty star-forming galaxies without emission lines in their optical spectra because of strong dust extinction.

4.2. Environmental Dependence of the 12 μm LF: Early-type Galaxies with MIR Emission

In Figure 13(c), the early-type galaxies also show an "MIR star-forming sequence" consisting of SF galaxies, known as star-forming (or blue), early-type galaxies (e.g., Fukugita et al. 2004; Lee et al. 2006, 2010). We check their optical color images and their positions in the optical color–magnitude diagrams. This inspection confirms that they are indeed morphologically early-type galaxies with blue colors. However, most early-type galaxies form an "MIR blue cloud" in the low-luminosity regime (i.e., $\nu L_\nu(12\,\mu\text{m}) \lesssim 5 \times 10^8\ h_{70}^{-2}\ L_\odot$); this cloud is mainly responsible for the faint-end slope of 12 μm LFs. Most of the spectral types for these galaxies are "undetermined" because there are no emission lines in the optical spectra, and they show a wide spread in MIR colors at [3.4]–[12] < -0.7. Their SEDs are consistent with passively evolving, old stellar populations with weak MIR emission (weak MIR-excess galaxies) resulting from the circumstellar dust envelopes around AGB stars (Ko et al. 2009, 2012; see Figure 4 in Shim et al. 2011). These galaxies usually form a tight red sequence in the optical color–magnitude diagram, indicating a homogeneous population, but they show a wide spread in MIR colors depending on their stellar age. In panel (c), we overplot the predictions from Single Stellar Population (SSP) models with different ages, which include the MIR emission from the AGB dust (Piovan et al. 2003). Model predictions with mean stellar ages greater than ~5 Gyr are consistent with the colors of these weak MIR-excess galaxies.

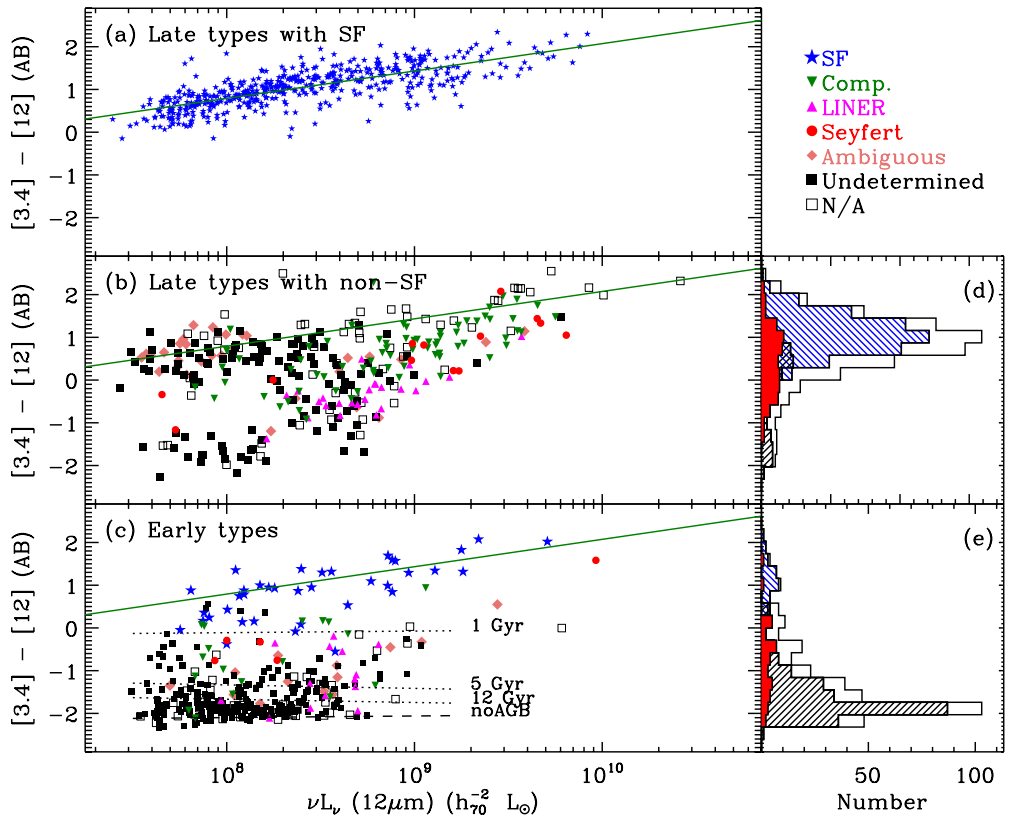

Figure 13. MIR color–luminosity diagrams for late-type galaxies with SF spectral type (a) and with non-SF spectral type (b), and for early-type galaxies (c) in the A2199 supercluster. Different symbols indicate different optical spectral types. Green solid lines are the linear fit to late-type galaxies with star formation. Dotted lines indicate model predictions calculated from the AGB model SSPs (Piovan et al. 2003), assuming a metallicity sequence at three different stellar ages (1, 5, and 12 Gyr), respectively. The horizontal dashed line represents the model SSP without AGB dust. (d) Histograms of MIR colors for late-type, AGN-host (Seyferts, LINERs, and composites) galaxies (red), SF galaxies (hatched one with orientation of 315° (\\ with blue colors)), quiescent (undetermined) galaxies (hatched one with orientation of 45° (// with black colors)), and total sample (open one with black colors). (e) Same as (d), but for early-type galaxies.

(A color version of this figure is available in the online journal.)

To check the radial distribution of these early-type galaxies, we plot [3.4]–[12] colors and the fraction of these weak MIR-excess galaxies among 12 μm emitters as a function of clustercentric radius in Figure 14. Panels (a) and (b) show a clear [3.4]–[12] color segregation depending on galaxy morphology at all the clustercentric radii. There is a concentration of early-type galaxies with weak MIR emission in the inner region of the cluster ($R \lesssim 100' \approx 2.5\ h^{-1}$ Mpc $\approx 2.5 r_{200,\mathrm{A2199}}$). Panel (c) shows that the fraction of these weak MIR-excess galaxies among 12 μm emitters starts to increase with decreasing clustercentric radius at $\sim$100′ both for early types and for the total sample (see also Haines et al. 2006 based on the optical spectral analysis). This trend is similar to the radial variation of the early-type fraction shown in panel (d). These results suggest that the weak MIR-excess galaxies (mostly early types) that are within the virial radius of A2199 as well as at the infall region (i.e., $R \approx 1 - 3 r_{200,\mathrm{A2199}}$), are responsible for the steep faint-end slope of 12 μm LFs in the inner region.

Cluster, early-type galaxies with MIR emission were found in other studies (e.g., Ko et al. 2009; Shim et al. 2011; Clemens et al. 2011). For example, Bressan et al. (2006) observed 17 Virgo early-type galaxies with the *Spitzer* Infrared Spectrograph, and suggested that 76% of their sample are passively evolving galaxies with a broad silicate feature, consistent with the emission from dusty circumstellar envelopes of mass-losing, evolved stars. In the Coma cluster, Clemens et al. (2009) found that the majority (68%) of the early-type galaxies have MIR and optical colors consistent with SSP models with dusty AGB envelopes. Of course, there are also early-type galaxies with MIR emission in the field (Kaneda et al. 2008; Panuzzo et al. 2011). These studies provide a hint that the fraction of weak MIR-excess galaxies is lower in the field than in cluster regions (Figure 13(b)), but an extensive comparison with a larger sample is important.

Interestingly, the fraction of weak MIR-excess galaxies for late types in panel (c) of Figure 14 increases only in the very inner region of the cluster ($R \lesssim 20' \approx 0.5\ h^{-1}$ Mpc $\approx 0.5 r_{200,\mathrm{A2199}}$). These late-type, weak MIR-excess galaxies are similar to "passive spirals" that are also observed in other clusters at intermediate redshifts. These galaxies may be progenitors of S0 galaxies (e.g., Couch et al. 1998; Moran et al. 2007). The existence of these late-type, weak MIR-excess galaxies in the central cluster region means that their SFA is suppressed, but their morphologies remain late types. This result indicates an important role for hydrodynamic processes (that are not effective in changing galaxy structure) including ram pressure (Gunn & Gott 1972), strangulation (Larson et al. 1980), and galaxy–galaxy hydrodynamic interactions (Park & Hwang 2009) in the quenching of SFA in these central regions of clusters. On the other hand, the physical processes related to the quenching of SFA and the morphological transformation of cluster galaxies may work over different timescales (i.e., there may be faster changes in SFA than the morphological transformation; e.g., Poggianti et al. 1999; Moran et al. 2007; Sánchez-Blázquez et al. 2009).

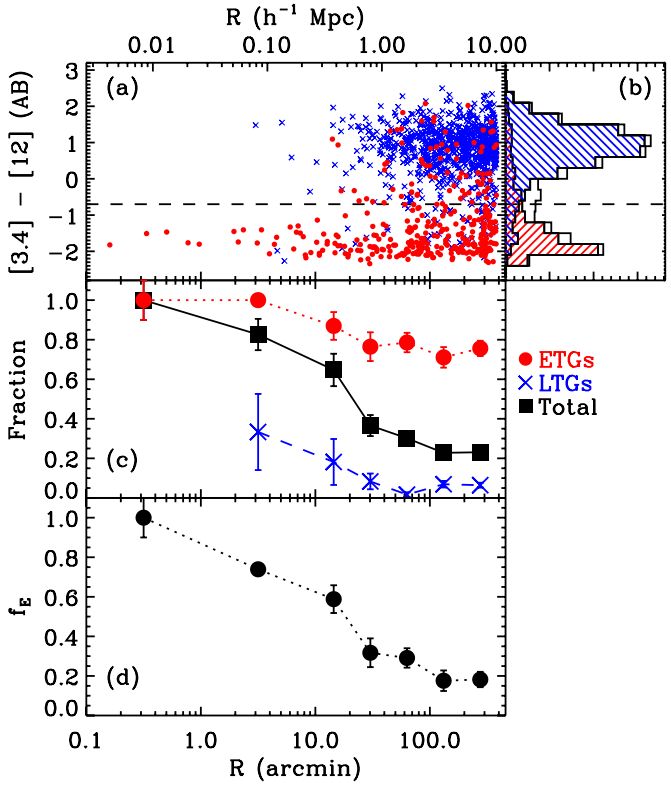

Figure 14. (a) [3.4]–[12] (AB), (c) the fraction of weak MIR-excess galaxies (i.e., [3.4]–[12] < -0.7), and (d) the early-type fraction (f_E) for galaxies in the A2199 supercluster with $m_r \leqslant -17$ as a function of clustercentric radius. (b) Histograms of MIR colors for early-type (hatched one with orientation of 45° (// with red colors)) and late-type galaxies (hatched one with orientation of 315° (\\ with blue colors)), and total sample (open one with black colors). Red circles and blue crosses in (a) and (c) are for early- and late-type galaxies, respectively, and black squares are for the total sample. Error bars indicate Poisson uncertainties.

(A color version of this figure is available in the online journal.)

5. CONCLUSIONS

Using the homogeneous data set of *WISE* and SDSS that covers the entire supercluster region, we examine the MIR properties of supercluster galaxies. Our primary results are as follows.

1. The MIR colors ([3.4]–[12]) of late-type, star-forming galaxies correlate strongly with 12 μm luminosity. These galaxies trace out a star-forming sequence in the MIR color–luminosity diagram.
2. MIR-detected (i.e., *WISE* 22 μm or 12 μm) galaxies tend to be more metal-rich and to have higher surface brightness than non-MIR detections at a fixed SFR.

Using these MIR-detected galaxies at 22 μm or 12 μm, we investigate the IR LFs and their environmental dependence in the supercluster. The main results are as follows.

1. The TIR LFs are dominated by late-type, star-forming galaxies. The contribution of AGN hosts increases with increasing IR luminosity. Similarly, late-type, non-AGN galaxies dominate 12μm LFs; the contribution of early-type galaxies increases with decreasing 12 μm luminosity.
2. The faint-end slope of TIR LFs does not change with environment. However, the faint-end slope in the 12 μm LFs varies with the environment. The faint-end slope in the dense inner cluster region is steeper than that in the less dense outer region. This behavior results primarily from the increasing contribution of early-type galaxies to the faint end of 12 μm LFs with decreasing clustercentric radius. These early-type galaxies contain passively evolving, old stellar populations with weak MIR emission from AGB dust.

The combination of the wide-field survey data set of *WISE* and spectroscopic surveys covering the entire region of the A2199 supercluster provides a unique opportunity to study the MIR properties of supercluster galaxies and their environmental dependence. A detailed view of SF and nuclear activity for these supercluster galaxies will be studied in a forthcoming paper (G.-H. Lee et al., in preparation). The combination of *WISE* all-sky survey data and the Hectospec Cluster Survey data (K. Rines et al., in preparation) will provide data for extending this study to other cluster systems.

We thank the anonymous referee for constructive comments that helped us to improve the manuscript. We thank Scott Kenyon for carefully reading the manuscript. We also thank Gwang-Ho Lee, David Elbaz, Jongwan Ko, Minjin Kim, Jong Chul Lee, Jubee Sohn, and Hyunjin Shim for useful discussion. H.S.H. acknowledges the Smithsonian Institution for the support of his post-doctoral fellowship. The Smithsonian Institution also supports M.J.G.'s research. A.D. acknowledges partial support from the INFN grant PD51 and the PRIN-MIUR-2008 grant 2008NR3EBK_003 "Matter-antimatter asymmetry, dark matter and dark energy in the LHC era." K.R. was funded in part by a Cottrell College Science Award from the Research Corporation. This publication makes use of data products from the *Wide-field Infrared Survey Explorer*, which is a joint project of the University of California, Los Angeles, and the Jet Propulsion Laboratory/California Institute of Technology, funded by the National Aeronautics and Space Administration.

REFERENCES

Abazajian, K. N., Adelman-McCarthy, J. K., Agüeros, M. A., et al. 2009, ApJS, 182, 543
Assef, R. J., Kochanek, C. S., Brodwin, M., et al. 2010, ApJ, 713, 970
Atlee, D. W., & Martini, P. 2012, ApJ, submitted (arXiv:1201.2957)
Bai, L., Rieke, G. H., Rieke, M. J., Christlein, D., & Zabludoff, A. I. 2009, ApJ, 693, 1840
Bai, L., Rieke, G. H., Rieke, M. J., et al. 2006, ApJ, 639, 827
Baldwin, J. A., Phillips, M. M., & Terlevich, R. 1981, PASP, 93, 5
Benson, A. J., Bower, R. G., Frenk, C. S., et al. 2003, ApJ, 599, 38
Biviano, A., Fadda, D., Durret, F., Edwards, L. O. V., & Marleau, F. 2011, A&A, 532, A77
Blanton, M. R., Dalcanton, J., Eisenstein, D., et al. 2001, AJ, 121, 2358
Blanton, M. R., & Moustakas, J. 2009, ARA&A, 47, 159
Böhringer, H., Voges, W., Huchra, J. P., et al. 2000, ApJS, 129, 435
Boselli, A., & Gavazzi, G. 2006, PASP, 118, 517
Bressan, A., Granato, G. L., & Silva, L. 1998, A&A, 332, 135
Bressan, A., Panuzzo, P., Buson, L., et al. 2006, ApJ, 639, L55
Brinchmann, J., Charlot, S., White, S. D. M., et al. 2004, MNRAS, 351, 1151
Carlberg, R. G., Yee, H. K. C., & Ellingson, E. 1997, ApJ, 478, 462
Charlot, S., & Fall, S. M. 2000, ApJ, 539, 718
Chary, R., & Elbaz, D. 2001, ApJ, 556, 562
Choi, Y., Han, D., & Kim, S. S. 2010, J. Korean Astron. Soc., 43, 191
Chung, S. M., Eisenhardt, P. R., Gonzalez, A. H., et al. 2011, ApJ, 743, 34
Chung, S. M., Gonzalez, A. H., Clowe, D., Markevitch, M., & Zaritsky, D. 2010, ApJ, 725, 1536
Clemens, M. S., Bressan, A., Panuzzo, P., et al. 2009, MNRAS, 392, 982
Clemens, M. S., Panuzzo, P., Rampazzo, R., Vega, O., & Bressan, A. 2011, MNRAS, 412, 2063
Cortese, L., Boselli, A., Gavazzi, G., et al. 2005, ApJ, 623, L17
Cortese, L., Gavazzi, G., & Boselli, A. 2008, MNRAS, 390, 1282
Couch, W. J., Barger, A. J., Smail, I., Ellis, R. S., & Sharples, R. M. 1998, ApJ, 497, 188

Davis, M., & Geller, M. J. 1976, ApJ, 208, 13
Diaferio, A. 1999, MNRAS, 309, 610
Diaferio, A., & Geller, M. J. 1997, ApJ, 481, 633
Donoso, E., Yan, L., Tsai, C., et al. 2012, ApJ, 748, 80
Draine, B. T., & Li, A. 2007, ApJ, 657, 810
Dressler, A. 1980, ApJ, 236, 351
Elbaz, D., Daddi, E., Le Borgne, D., et al. 2007, A&A, 468, 33
Elbaz, D., Dickinson, M., Hwang, H. S., et al. 2011, A&A, 533, A119
Elbaz, D., Hwang, H. S., Magnelli, B., et al. 2010, A&A, 518, L29
Fang, F., Shupe, D. L., Xu, C., & Hacking, P. B. 1998, ApJ, 500, 693
Finn, R. A., Desai, V., Rudnick, G., et al. 2010, ApJ, 720, 87
Fukugita, M., Nakamura, O., Turner, E. L., Helmboldt, J., & Nichol, R. C. 2004, ApJ, 601, L127
Gallazzi, A., Bell, E. F., Wolf, C., et al. 2009, ApJ, 690, 1883
Geller, M. J., Diaferio, A., Kurtz, M. J., Dell'Antonio, I. P., & Fabricant, D. G. 2012, AJ, 143, 102
Goto, T., Arnouts, S., Inami, H., et al. 2011a, MNRAS, 410, 573
Goto, T., Arnouts, S., Malkan, M., et al. 2011b, MNRAS, 414, 1903
Gunn, J. E., & Gott, J. R., III 1972, ApJ, 176, 1
Haines, C. P., Busarello, G., Merluzzi, P., et al. 2011, MNRAS, 412, 127
Haines, C. P., La Barbera, F., Mercurio, A., Merluzzi, P., & Busarello, G. 2006, ApJ, 647, L21
Heckman, T. M., Robert, C., Leitherer, C., Garnett, D. R., & van der Rydt, F. 1998, ApJ, 503, 646
Hwang, H. S., Elbaz, D., Lee, J. C., et al. 2010, A&A, 522, A33
Hwang, H. S., Park, C., Elbaz, D., & Choi, Y.-Y. 2012, A&A, 538, A15
Iglesias-Páramo, J., Boselli, A., Cortese, L., Vílchez, J. M., & Gavazzi, G. 2002, A&A, 384, 383
Jarrett, T. H., Cohen, M., Masci, F., et al. 2011, ApJ, 735, 112
Johnstone, R. M., Allen, S. W., Fabian, A. C., & Sanders, J. S. 2002, MNRAS, 336, 299
Kaneda, H., Onaka, T., Sakon, I., et al. 2008, ApJ, 684, 270
Kauffmann, G., Heckman, T. M., Tremonti, C., et al. 2003, MNRAS, 346, 1055
Kelson, D. D., & Holden, B. P. 2010, ApJ, 713, L28
Kelson, D. D., Zabludoff, A. I., Williams, K. A., et al. 2002, ApJ, 576, 720
Kennicutt, R. C., Jr. 1998, ARA&A, 36, 189
Kewley, L. J., Dopita, M. A., Sutherland, R. S., Heisler, C. A., & Trevena, J. 2001, ApJ, 556, 121
Kewley, L. J., Groves, B., Kauffmann, G., & Heckman, T. 2006, MNRAS, 372, 961
Knobel, C., Lilly, S. J., Iovino, A., et al. 2009, ApJ, 697, 1842
Ko, J., Im, M., Lee, H. M., et al. 2009, ApJ, 695, L198
Ko, J., Im, M., Lee, H. M., et al. 2012, ApJ, 745, 181
Koyama, Y., Kodama, T., Shimasaku, K., et al. 2010, MNRAS, 403, 1611
Larson, R. B., Tinsley, B. M., & Caldwell, C. N. 1980, ApJ, 237, 692
Lee, J. H., Hwang, H. S., Lee, M. G., Lee, J. C., & Matsuhara, H. 2010, ApJ, 719, 1946
Lee, J. H., Lee, M. G., & Hwang, H. S. 2006, ApJ, 650, 148
Lee, J. C., et al. 2011, ApJ, submitted
Leroy, A. K., Bolatto, A., Gordon, K., et al. 2011, ApJ, 737, 12
Li, H.-N., Wu, H., Cao, C., & Zhu, Y.-N. 2007, AJ, 134, 1315
Magdis, G. E., Daddi, E., Elbaz, D., et al. 2011, ApJ, 740, L15
Markwardt, C. B. 2009, in ASP Conf. Ser. 411, Astronomical Data Analysis Software and Systems XVIII, ed. D. A. Bohlender, D. Durand, & P. Dowler (San Francisco, CA: ASP), 251
Metcalfe, L., Fadda, D., & Biviano, A. 2005, Space Sci. Rev., 119, 425
Moore, B., Katz, N., Lake, G., Dressler, A., & Oemler, A. 1996, Nature, 379, 613
Moran, S. M., Ellis, R. S., Treu, T., et al. 2007, ApJ, 671, 1503
Mullaney, J. R., Alexander, D. M., Goulding, A. D., & Hickox, R. C. 2011, MNRAS, 414, 1082
Murakami, H., Baba, H., Barthel, P., et al. 2007, PASJ, 59, 369
Netzer, H., Lutz, D., Schweitzer, M., et al. 2007, ApJ, 666, 806
Noeske, K. G., Weiner, B. J., Faber, S. M., et al. 2007, ApJ, 660, L43
Oemler, A., Jr. 1974, ApJ, 194, 1
Oyaizu, H., Lima, M., Cunha, C. E., et al. 2008, ApJ, 674, 768
Panuzzo, P., Rampazzo, R., Bressan, A., et al. 2011, A&A, 528, A10
Park, C., & Choi, Y. 2005, ApJ, 635, L29
Park, C., Choi, Y., Vogeley, M. S., Gott, J. R. I., & Blanton, M. R. 2007, ApJ, 658, 898
Park, C., & Hwang, H. S. 2009, ApJ, 699, 1595
Peebles, P. J. E. 1993, Principles of Physical Cosmology (Princeton, NJ: Princeton Univ. Press)
Pérez-González, P. G., Rieke, G. H., Egami, E., et al. 2005, ApJ, 630, 82
Pilbratt, G. L., Riedinger, J. R., Passvogel, T., et al. 2010, A&A, 518, L1
Piovan, L., Tantalo, R., & Chiosi, C. 2003, A&A, 408, 559
Poggianti, B. M., Smail, I., Dressler, A., et al. 1999, ApJ, 518, 576
Rieke, G. H., Alonso-Herrero, A., Weiner, B. J., et al. 2009, ApJ, 692, 556
Rines, K., & Geller, M. J. 2008, AJ, 135, 1837
Rines, K., Geller, M. J., Diaferio, A., et al. 2002, AJ, 124, 1266
Rines, K., Mahdavi, A., Geller, M. J., et al. 2001, ApJ, 555, 558
Ryder, S. D. 1995, ApJ, 444, 610
Salpeter, E. E. 1955, ApJ, 121, 161
Sánchez-Blázquez, P., Jablonka, P., Noll, S., et al. 2009, A&A, 499, 47
Sanders, D. B., Mazzarella, J. M., Kim, D., Surace, J. A., & Soifer, B. T. 2003, AJ, 126, 1607
Schechter, P. 1976, ApJ, 203, 297
Serra, A. L., Angus, G. W., & Diaferio, A. 2010, A&A, 524, A16
Serra, A. L., Diaferio, A., Murante, G., & Borgani, S. 2011, MNRAS, 412, 800
Shim, H., Im, M., Lee, H. M., et al. 2011, ApJ, 727, 14
Shioya, Y., Taniguchi, Y., Sasaki, S. S., et al. 2008, ApJS, 175, 128
Simon, J. D., Prada, F., Vílchez, J. M., Blitz, L., & Robertson, B. 2006, ApJ, 649, 709
Smith, J. D. T., Draine, B. T., Dale, D. A., et al. 2007, ApJ, 656, 770
Spinoglio, L., & Malkan, M. A. 1989, ApJ, 342, 83
Stoughton, C., Lupton, R. H., Bernardi, M., et al. 2002, AJ, 123, 485
Tran, K.-V. H., Saintonge, A., Moustakas, J., et al. 2009, ApJ, 705, 809
Tremonti, C. A., Heckman, T. M., Kauffmann, G., et al. 2004, ApJ, 613, 898
Veilleux, S., & Osterbrock, D. E. 1987, ApJS, 63, 295
Werner, M. W., Roellig, T. L., Low, F. J., et al. 2004, ApJS, 154, 1
Westra, E., Geller, M. J., Kurtz, M. J., Fabricant, D. G., & Dell'Antonio, I. 2010, ApJ, 708, 534
Wright, E. L., Eisenhardt, P. R. M., Mainzer, A. K., et al. 2010, AJ, 140, 1868
York, D. G., Adelman, J., Anderson, J. E., Jr., et al. 2000, AJ, 120, 1579